Science Advances
AAAS

# Supplementary Materials for

## Binder-free printed PEDOT wearable sensors on everyday fabrics using oxidative chemical vapor deposition

Michael Clevenger, Hyeonghun Kim, Han Wook Song, Kwangsoo No, Sunghwan Lee*

*Corresponding author. Email: sunghlee@purdue.edu

Published 15 October 2021, *Sci. Adv.* **7**, eabj8958 (2021)
DOI: 10.1126/sciadv.abj8958

**This PDF file includes:**

## Section S1. Methods

### *Bending Test:*

The bending test was conducted by measuring sheet resistance utilizing a four-point probe before and after certain bending cycles. Fabrics were secured to a flat piece of glass, and then one end was lifted and bent with a bending angle of approximately 180°, then resecured. After each bending cycle, sheet resistance was measured. As a reference, the conductivity of oCVD PEDOT films was recorded as well from samples deposited on glass substrates.

### *FTIR:*

Chemical bonding information was analyzed utilizing Fourier-Transform Infrared Spectroscopy (FTIR). FTIR spectra were obtained utilizing a Nexus 670 ThermoNicolet Spectrometer with an Attenuated Total Reflection (ATR) accessory. Bonding information was compared between PEDOT deposited on Si and fabric substrates. Bare Si and fabric substrates were used for background scans and the resulting FTIR spectra exclude the substrate information.

### *AFM:*

Surface topography information and root mean square (RMS) roughness of PEDOT deposited on Si substrates was obtained through an image area of 1 μm × 1 μm using tapping mode on a Veeco Dimension atomic force microscopy (AFM) with a Si cantilever (frequency 325 kHz).

### *SEM:*

Conformality and microstructures of oCVD PEDOT thin films on typical cotton fabrics were confirmed using images from a Thermo Fischer Scientific Teneo scanning electron microscope (SEM) with a magnification of approximately1500-2000×. oCVD PEDOT films of varying thicknesses deposited on fabric were compared to bare fabric to confirm film conformality.

Bare fabric was imaged in the Teneo SEM by utilizing its dedicated low vacuum secondary electron detector to aid in imaging of non-conductive samples. To compare the conformality and mechanical stability of oCVD PEDOT films, SEM micrographs of solution-processed PEDOT;PSS were also obtained.

***UV-Vis:***

Bandgap of PEDOT thin films was extracted through investigation of ultraviolet-visible regime absorption spectra using a Varian Cary 50 UV-Vis Spectrometer. Transparency data was also analyzed for thinner film oCVD PEDOT samples deposited on glass substrates (~30 nm film thickness).

***Breathability tests***:

The breathability test consisted of filling vials with 3 ml of deionized water. The fabric samples were then placed over the top opening of the vials and sealed around the edge through rubber banding. Vials were then placed equidistant from each other on a hot plate heated to 120 °C. The total mass of the vial, fabric, and water sample was measured in grams. At 2-hour, 4-hour, and 6-hour increments, the total mass was remeasured across a continuous 48-hour test. Breathability was then calculated via the difference in the initial volume of water present and the change in total mass (converted to volume) across the test. Breathability tests were conducted on PEDOT-deposited fabrics with the thickness of ~58 nm, 150 nm, and 350 nm. Measured PEDOT breathability was compared to the measured breathability of the bare fabric.

**Table S1.** Comparison of the performances of conductive polymer-based pressure sensors.

| Active materials | Sensitivity ($kPa^{-1}$) | Response Time (ms) | Recovery Time (ms) | Reference |
|---|---|---|---|---|
| oCVD PEDOT | 8 | 260 | 30 | This work |
| PEDOT:PSS coated Polyurethane | 0.3 $kPa^{-1}$ | - | - | 34 |
| PEDOT:PSS/SWCNT | 0.1 | 45 | 45 | 35 |
| Gelatin methacryloyl | 0.19 | 161 | 161 | 36 |
| PEDOT:PSS/PEDOT NWs/CNF | 1.59 | 360 | 200 | 37 |
| PEDOT:PSS coated PDMS | 21 | 90 | - | 38 |
| PEDOT:PSS/PAA on PDMS micropyramid | 39.9 | 49 | - | 39 |
| Polyurethane-cabon black mixture | 3.05 | 91 | 49 | 40 |
| Polypyrroe/Ag nanowire/PDMS/Polypyrrole | 28 | 280 | 53 | 41 |
| PEDOT:PSS/Graphene oxide | 0.548 | - | 250 | 42 |
| Poly(ionic liquid) nanofibrous membranes | 0.49 | - | 30 | 43 |
| Ag NP-Pedot_paper composite | 0.119 | 200 | 100 | 44 |
| PEDOT:PSS coated Melamine foam | | 97 | 56 | 45 |
| PVDF-HFP/PEDOT NF | 13.5 | 400 | 200 | 46 |
| GO-doped Polyuretane@PEDOT | 20.6 | 5 | 5 | 47 |

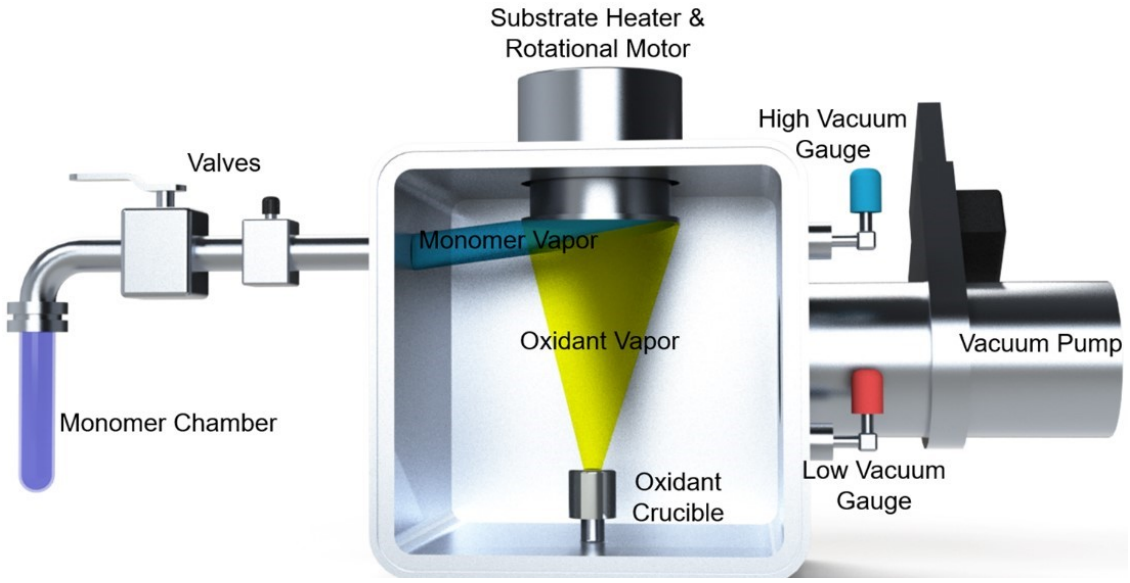


**Fig. S1.** An overall schematic of oCVD reactor.

The oCVD reactor is an enclosed sealed chamber that maintains conditions to allow for vapor phase polymerization of PEDOT, monomers are stored in a glass holding chamber that is then heated via a thermal heating jacket to the vaporization temperature of the monomer. The monomer is then introduced via a valve system that controls the rate of vapor introduction into the chamber. The oxidizing agent is stored in a crucible in the main chamber that is heated to the agent's sublimation temperature during the deposition process. Substrates are held in an upside-down holder that contains a heater and a rotational motor. Chamber vacuum pressure is monitored using low and high vacuum gauges. Synthesis of PEDOT thin films was done through the reaction of commercially available liquid EDOT and powdered iron (III) chloride ($FeCl_3$). Deposition pressures of $2\times10^{-3}$ Torr were achieved through the use of a combined roughing and turbo pumping system. EDOT monomer was introduced into the chamber using a needle valve after being heated to 130 °C to vaporize. $FeCl_3$ oxidizing agent was introduced after the powder was sublimated from a crucible via slow controlled heating to 180 °C at a ramping rate of approximately 10 °C per

minute. Once both the vaporized monomer and oxidizing agent were introduced into the chamber the heated substrates were uncovered through the use of a shutter system and were kept at a rotation speed of 5 rpm throughout deposition to result in uniform and homogeneous PEDOT films.

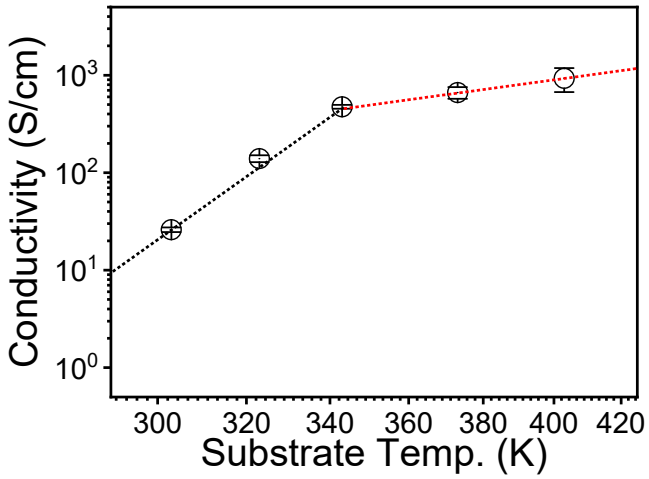


**Fig. S2.** Conductivity of oCVD PEDOT depending on deposition temperature.

The deposition temperature effect on the conductivity of oCVD PEDOT was investigated by growing the polymer film on a glass substrate. The use of glass substrates instead of the fabrics is to objectively measure the conductivity of oCVD PEDOT films on typical substrates (i.e., flat non-conductive substrates) and also to exclude the thermal degradation of the fabrics during the oCVD process. The relation between temperature ($T$) and conductivity ($\sigma$) was plotted as a log($\sigma$) vs. log($T$) as shown in Fig. S2. The log($\sigma$) linearly increased with increasing the temperature. Above the certain critical point (100 °C), the slope became slightly gentle but still steadily increased with the temperature.

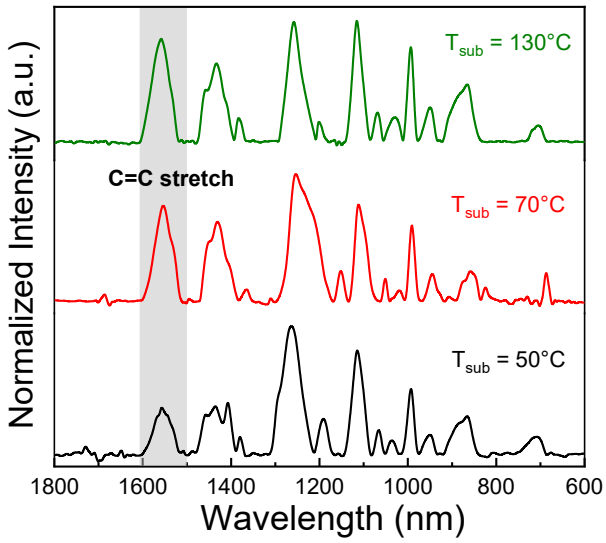


**Fig. S3.** FTIR spectra of oCVD PEDOT depending on deposition temperature.

Among other factors determining the conductivity of conjugated polymers, the conjugation length is of pivotal importance. To examine the possible effect of substrate temperature on the conjugation length of oCVD PEDOT, we analyzed 50 nm-thick PEDOT films, deposited at three different temperatures (50, 70, and 130 °C), using Fourier-transform infrared spectroscopy (FTIR). As shown in Fig. S3, the peak at around 1520 $cm^{-1}$, representing C=C stretching mode, tends to intensify with increasing substrate temperature. It is well known that the areal intensity of the C=C stretch peak is regarded as a valuable indicator to compare conjugation lengths as well as doping levels of PEDOT; the stronger peak is attributed to the longer conjugation length (*30-32*). Therefore, our FTIR results prove that a high-temperature surrounding facilitates the chain growth during the oCVD vapor-phase polymerization. Notably, the peak was intensified by raising the substrate temperature from 323 K to 343 K, whereas a lack of change was observed at higher temperatures. Thus, we can conclude that the conjugation and doping level of oCVD PEDOT is a strong function of the deposition temperature, and reaches a maximum level of conjugation and doping at a certain temperature, which is ~343 K. The temperature-dependent

doping level is supported by our previous reports (*30, 32*) that experimentally verified the high carrier concentrations in oCVD PEDOT through Hall effect measurements, of which the carrier density increases with increasing substrate temperature and the density reaches the theoretical maximum carrier density (~$2\times10^{21}$ $cm^{-3}$) at a substrate temperature of 70 °C or higher. Therefore, the conductivity trend conversion in Fig. S2 is likely attributed to the dependency of the doping level on the substrate temperature.

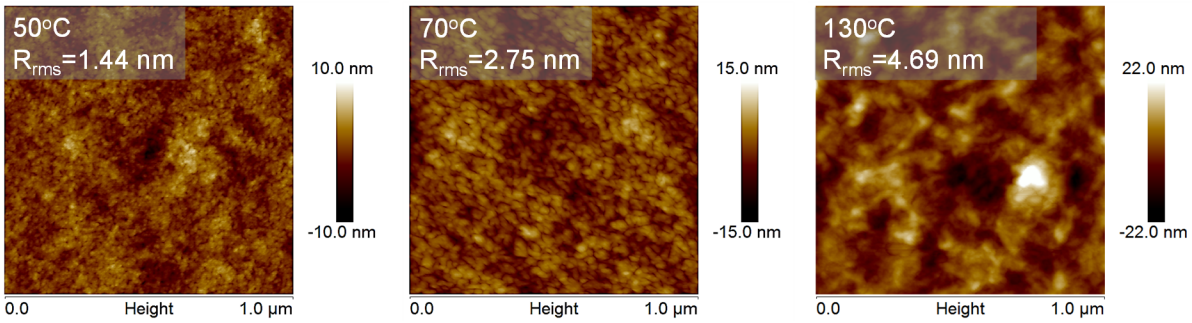


**Fig. S4.** AFM images of oCVD PEDOT depending on deposition temperature.

The crystallinity of polymer films is another significant factor dominating the charge transport property of PEDOT. We previously reported that resulting oCVD PEDOT films are in the nanocrystalline state (*30*). Herein, to investigate the crystalline grain size depending on the deposition temperature, the surface topological information of the PEDOT was analyzed using atomic force microscope (AFM), as shown in Fig. S4. The film roughness was gradually increased from 1.44 to 4.69 nm by raising the deposition temperature from 50 to 130 °C, implying that the size of the grain-like structures of the film could be enlarged under a high-temperature condition. The larger grain size obtained at higher substrate temperatures may enhance the charge carrier transport, which contributes to the increase in conductivity of oCVD PEDOT with substrate temperature. In addition to the enhanced conjugation and doping level in oCVD PEDOT with increasing substrate temperature (Fig. S3), the correlation between the grain size and the substrate temperate supports the conductivity results where higher substrate temperatures result in higher conductivity of oCVD PEDOT (*30, 31*).

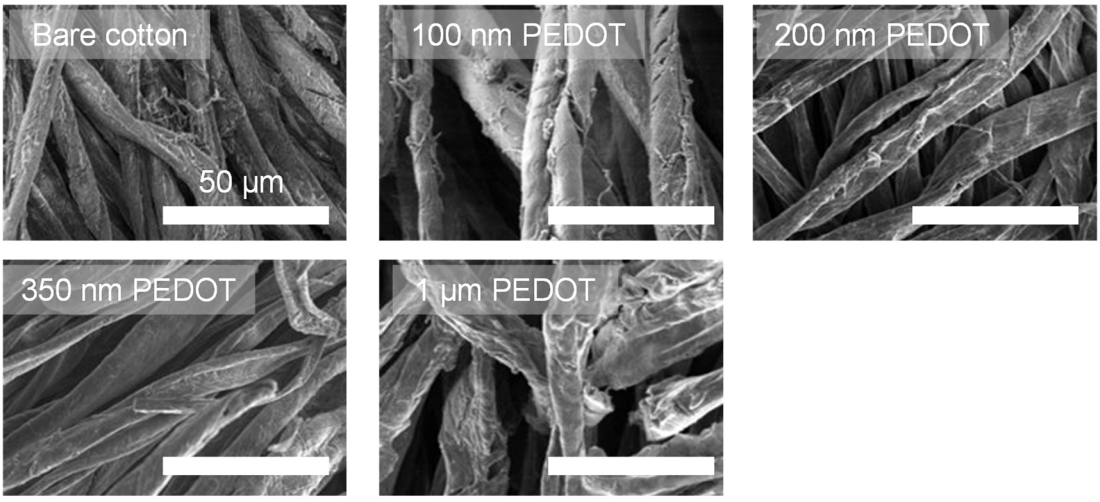


**Fig. S5.** SEM images of bare and PEDOT-coated fabrics with different polymer thickness.

Fig. S3 compare SEM images of fabrics with 100 nm, 200 nm, 350 nm, and 1 µm of deposited oCVD PEDOT with the bare fabric. The bare fabric has a rough surface with a substantial number of smaller strands covering the fabric threads. As PEDOT is deposited, the profiles of these smaller strands begin to smooth, as the thickness reaches a point where it is significantly greater that the topography of the strand. Even still, though the thickness of the film was increased, and surface topography of the fabric threads became smoother as film thickness increased, oCVD PEDOT still coats the fabric threads conformally no matter the film thickness in this study. This shows oCVD PEDOT's excellent conformality as only minor topographical differences are observed between bare fabric and coated fabrics with PEDOT films of 100, 200, 350 and 1000 nm, and the overall conformality of oCVD PEDOT around the thread is still clearly visible, regardless of film thickness, shown up to 1000 nm in this study.

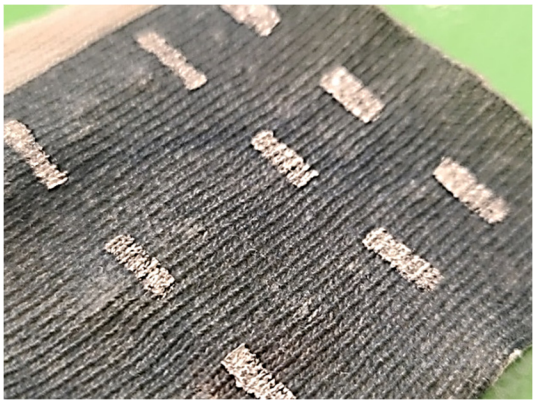

**Fig. S6.** A photo image of Ag paste electrodes, captured after PI tape masks removed. Photo Credit: Hyeonghun Kim, Purdue University

For the uniformity test, we used silver (Ag) paste as the conductive electrode and polyimide (PI) tape as a shadow mask to define a channel dimension for transmission line measurements (TLM). The TLM device structures were fabricated as follows; i) A PI mask having square holes, in which the electrode would be formulated, was prepared; ii) After attaching the mask to the fabric sample, silver paste solution was applied onto the exposed regions of the fabric through the mask; iii) The sample was completely dried under ambient condition for 1 hr. A photograph of the fabricated TLM structure is shown below and added to the supplementary materials as Fig. S6, which demonstrates electrode pairs placed on an oCVD PEDOT coated polyester fabric. The image was captured after detaching the mask, although the real electrical measurements were made with the PI mask in place.

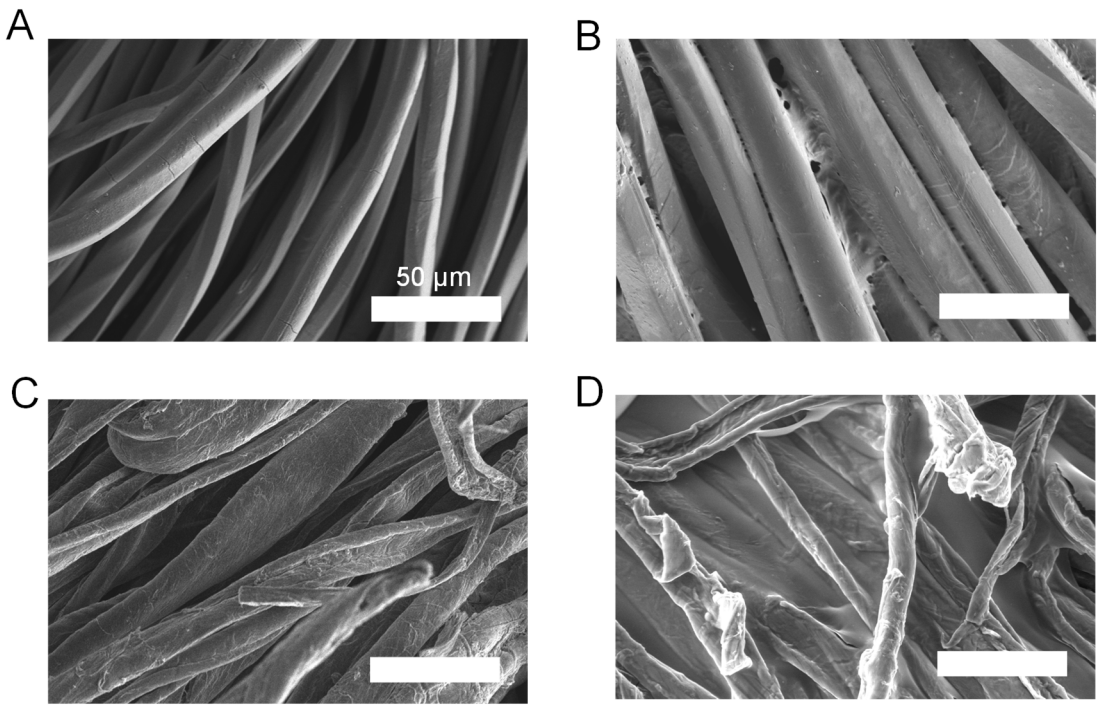


**Fig. S7. SEM images of oCVD PEDOT and PEDOT:PSS coated fabrics.** (**A**) oCVD PEDOT and (B) PEDOT:PSS on nylon. (**C**) oCVD PEDOT and (D) PEDOT:PSS on Cotton.

To investigate the universal conformability of the oCVD technique for versatile fabrics, we conducted SEM analysis on PEDOT and PEDOT:PSS on nylon and cotton fabrics. The thickness of oCVD PEDOT was adjusted to 200 nm. oCVD PEDOT uniformly covers both substrates. However, solution-processed PEDOT:PSS formed bridges between threads and filled gaps/pores in the fabric (i.e., reduced breathability). These results substantiate that the oCVD process can formulae a sensing layer while maintaining outstanding breathability and mechanical stability.

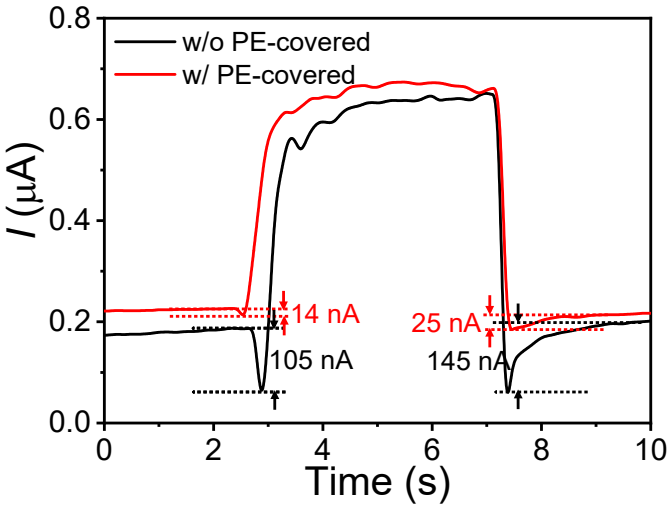


**Fig. S8.** A transient current change of the sensor, protected with and without a protection PE layer, under applying a pressure of 200 Pa.

To identify the origin of the sharp current drops in more detail, the sensor was tested with and without covering a polyester (PE) fabric on the PEDOT face, and the results were added to Fig. S8 in the supplementary materials. It is clearly evidenced that in the PEDOT sensor protected by PE, the transitory current drops were dramatically suppressed, compared to the PEDOT sensor in direct contact with glass without PE protection. The intensity of the current drops, defined here as the current difference between the local minimum at the moment of the initial pressure change and non-pressured state, decreased more than five times using the PE cap.

It is well known that glass is positively charged when contacted with other materials due to a typical triboelectric effect (*33*). The initial glass/PEDOT contact accompanies positive and negative charge generation on the glass and PEDOT, respectively. The generated transitory charge creates a triboelectric voltage across the PEDOT/glass interface, resulting in a signal interference representing the current drop. In general, the triboelectric phenomenon takes place in a short

moment (< 10 ms) and rapidly reaches an equilibrium state. Therefore, as shown in Fig. S8, the sensing response (current variation, recorded at the equilibrium state) was not significantly disturbed by the triboelectric effect. In the same manner, when we employ the sensor to monitor a blood pressure pattern from the wrist or neck, the triboelectric effect only occurs at the initial moment of touching the sensor on the body and disappears within several milliseconds; thus, a current change caused by blood pressure could be solely extracted.

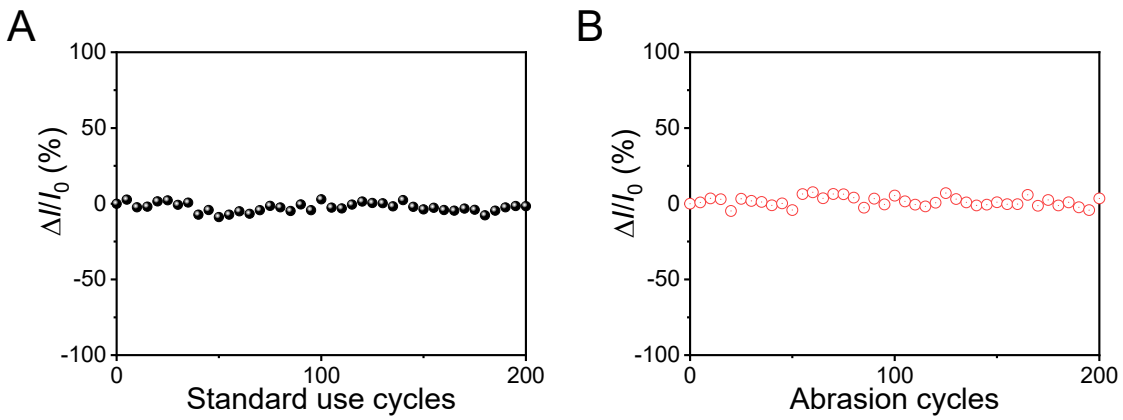


**Fig. S9. Sustainability tests.** Current change (**A**) after standard use and (**B**) abrasion tests.

To analyze the sustainability of our PEDOT fabric sensor against standard use as well as abrasion, the current change was measured against cycles of general use and intentional rubbing. In Fig. S9A, the change in current from initial measurements ($\Delta I/I_0$) was measured across 200 cycles of standard use, where the sensor was pressed against the skin, then the current was measured after removal to see if the repeated contact had any degrading effect on the resistance of the PEDOT film deposited on the fabrics. In Fig. S9B, the $\Delta I/I_0$ was again measured across 200 cycles of abrasion against human skin. In this experiment, the sensor was rubbed against human skin unidirectional for approximately 25mm. After removal from skin, current was measured with a voltage of 0.1V across each sensor, then reported at five cycle increments. Fig. S9A and B demonstrate that oCVD PEDOT deposited on fabric have good sustainability against both standard use and abrasion, where the ability to transfer current through the film was maintained and no signs of degradation due to repeated use or abrasion occurred.

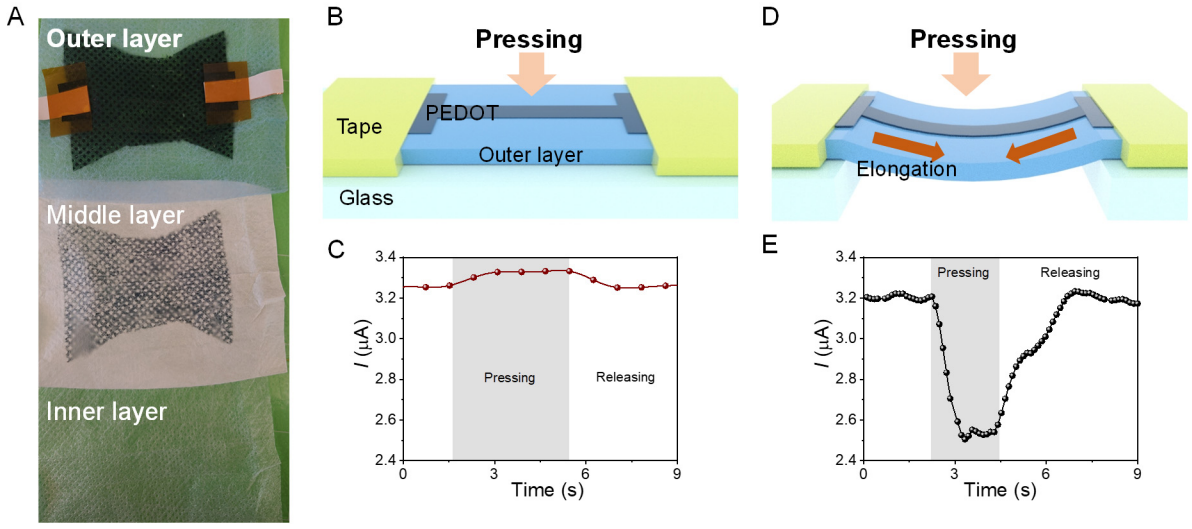


**Fig. S10. Investigation of the working principle of the oCVD PEDOT-based mask sensor.** (**A**) Photo images of three fabric layers in the mask after vapor-printing of oCVD PEDOT. The inset of Fig. S10A represents SEM image of the PEDOT coated outer layer. (**B**) A schematic and (**C**) transient current curve under a pressure of 1 kPa with a setup consisting of the outer layer of mask sensor entirely fixated on a compact glass. (**D**) A schematic and (**E**) transient current variation under the 1 kPa pressure with an experimental setup based on a floating fabric of which the two ends are fixated on glass substrates. Photo Credit: Hyeonghun Kim, Purdue University

The outermost non-woven facet among the three layers in a disposable mask was mainly covered by the oCVD PEDOT, while a discontinuous (hence highly resistive) PEDOT film was formulated on the middle fabric (Fig. S10A). In addition, the deposition of PEDOT was not observed in the innermost fabric due to the masking effect of the upper layers. Therefore, it is expected that the majority of current flows in the outer fabric. As such, we only utilized that outermost layer for investigating the working mechanism.

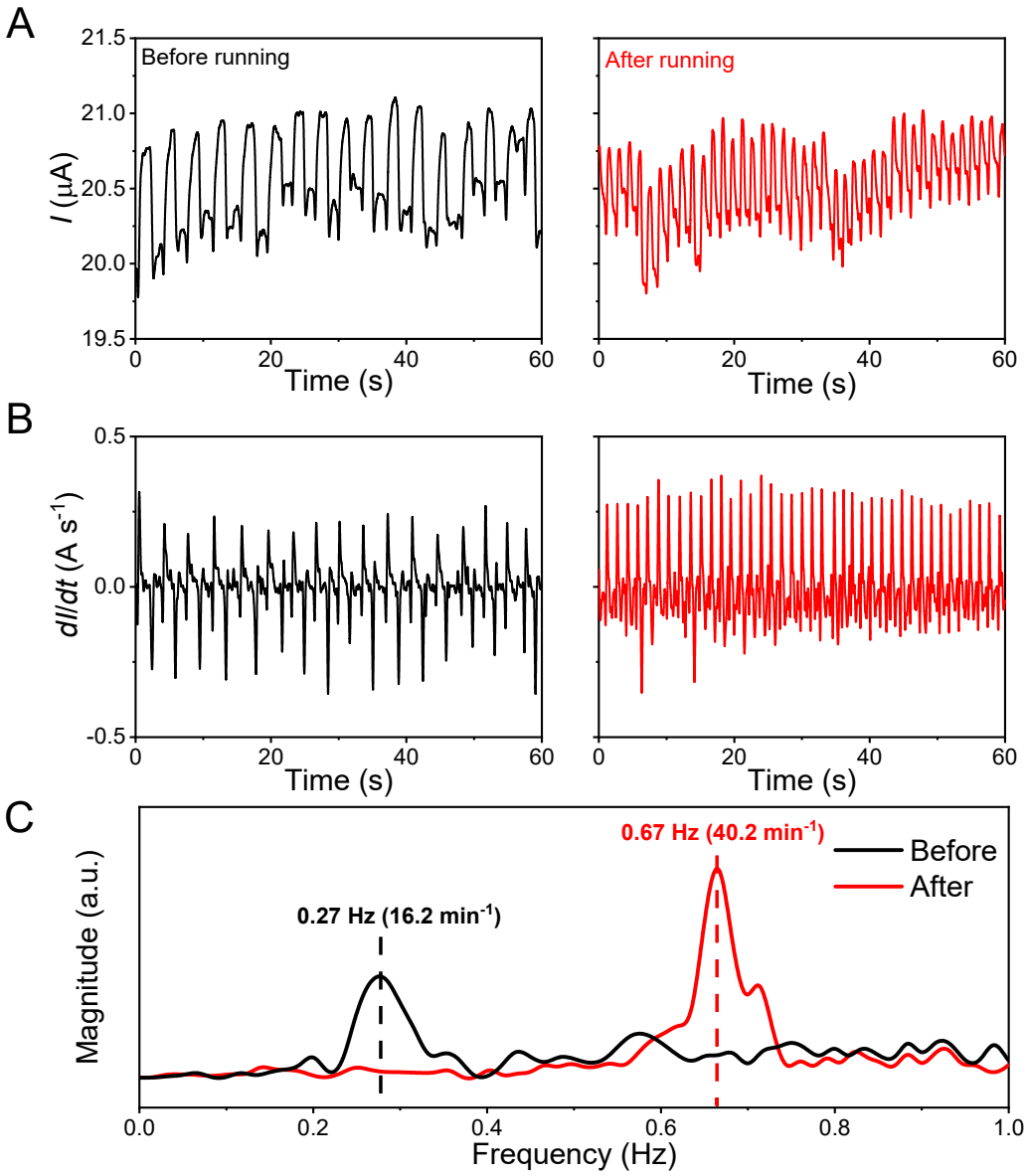


**Fig. S11. Signal processing for the mask sensor.** (**A**) Raw data, collected before and after exercise. (**B**) Differentiation of (A) in a time domain. (**C**) Fourier transformation of the result of (B).

Herein, we develop a mathematical protocol to correct a baseline shift and estimate an accurate respiratory rate in real-time. As shown in the raw data (Fig. S11A), the currents representing inhalation and exhalation states were fluctuated due to inconsistent tidal volume for each breath, and noise from the minute movement of the subject. To correct the undesired shifts, the results were differentiated with the time domain (Fig. S11B). This process serves as a role to

correct the baseline to be zero so that a current deviation caused by breath is selectively extracted. The next step is the Fourier transformation to convert the time-scale data to a frequency domain. Randomly released electrical noise or other possible errors derived by a human motion could be ignored in a specific frequency range of 0-1 Hz which contains respiratory pattern information (Fig. S11C). Therefore, as a consequence of the overall data processing series, precise respiratory rates were successfully estimated (16.2 and 40.2 min-1 for before and after running, respectively) as shown in Fig. S11C. It should be noted that the mathematical data processing renders quantitative analysis for respiratory rate even if uncontrollable variables from the environmental or human-dependent conditions affect the signal, thus ensuring reproducible data extraction.

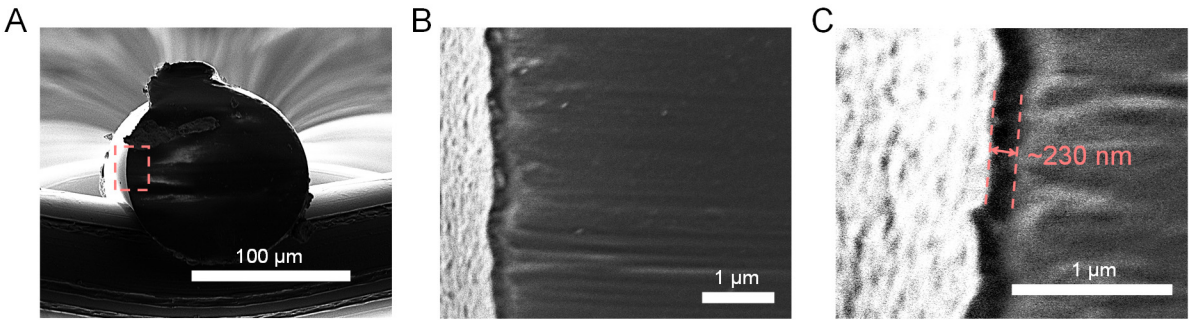


**Fig. S12. Thickness of the oCVD PEDOT directly measured from PEDOT-coated fabric.** (**A**) Low and (**B, C**) High magnification SEM images of the oCVD films deposited on a Nylon fabric

The thickness of the PEDOT film was measured through the common technique of measuring thickness of a reference sample (PEDOT on Silicon substrate) using an ellipsometer, that was deposited concomitantly. This technique is a well-documented method to examine thin film thickness information on substrates where direct measurement is difficult, but where a reference thickness sample on silicon can be measured with either an ellipsometer or profilometer (*55, 56*). Therefore, the thickness of the PEDOT film on fabric in the study is mentioned as the nominal thickness, as the true thickness measurement was measured on the silicon sample. To verify this technique, we have conducted additional measurements where cross-sectional images of PEDOT films deposited on fabric were measured via SEM and compared to ellipsometer measured reference samples deposited concomitantly with the fabric samples. The silicon reference sample measured with the ellipsometer reported a thickness 237 nm. SEM cross-sectional images of PEDOT films deposited on nylon fabric were obtained utilizing a Thermo Fischer Scientific Teneo. From the SEM images (Fig. S12), thickness information was measured along with multiple film locations, where the average film thickness was approximately 230 nm, showing less than 5% error between the SEM cross-sectional image and ellipsometer measurements of the silicon reference sample deposited concomitantly. This shows the validity of

the reference sample technique in measuring sample thicknesses where direct thickness measuring is difficult.

## REFERENCES AND NOTES


1. C. Wang, K. Xia, H. Wang, X. Liang, Z. Yin, Y. Zhang, Advanced carbon for flexible and wearable Electronics. *Adv. Mater.* **31**, 1801072 (2019).

2. M. Amjadi, K.-U. Kyung, I. Park, M. Sitti, Stretchable, skin-mountable, and wearable strain sensors and their potential applications: A review. *Adv. Funct. Mater.* **26**, 1678–1698 (2016).

3. Y. Liu, M. Pharr, G. A. Salvatore, Lab-on-skin: A review of flexible and stretchable electronics for wearable health monitoring. *ACS Nano* **11**, 9614–9635 (2017).

4. A. Nag, S. C. Mukhopadhyay, J. Kosel, Wearable flexible sensors: A review. *IEEE Sensors J.* **7**, 3949–3960 (2017).

5. Q. Li, L.-N. Zhang, X-.M. Tao, X. Ding, Review of flexible temperature sensing networks for wearable physiological monitoring. *Adv. Healthc. Mater.* **6**, 1601371 (2017).

6. A. Servati, L. Zou, Z. J. Wang, F. Ko, P. Servati, Novel flexible wearable sensor materials and signal processing for vital sign and human activity monitoring. *Sensors* **17**, 1622 (2017).

7. S. Seyedin, P. Zhang, M. Naebe, S. Qin, J. Chen, X. Wanga, J. M. Razal, Textile strain sensors: A review of the fabrication technologies, performance evaluation and applications. *Mater. Horiz.* **6**, 219–249 (2019).

8. J. S. Heo, J. Eom, Y.-H. Kim, S. K. Park, Recent progress of textile-based wearable electronics: A comprehensive review of materials, devices, and applications. *Small* **14**, 1703034 (2018).

9. G. Acar, O. Ozturk, A. J. Golparvar, T. A. Elboshra, K. Böhringer, M. K. Yapici, Wearable and flexible textile electrodes for biopotential signal monitoring: A review. *Electronics* **8**, 479 (2019).

10. K. Opwis, D. Knittel, J. S. Gutmann, Oxidative in situ deposition of conductive PEDOT:PTSA on textile substrates and their application as textile heating element. *Synth. Met.* **162**, 1912–1918 (2012).

11. A. Hebeish, S. Farag, S. Sharaf, T. I. Shaheen, Advancement in conductive cotton fabrics through in situ polymerization of polypyrrole-nanocellulose composites. *Carbohydr. Polym.* **151**, 96–102 (2012).

12. N. D. Tissera, R. N. Wijesena, S. Rathnayake, R. M. de Silva, K. M. N. de Silva, Heterogeneous in situ polymerization of polyaniline (PANI) nanofibers on cotton textiles: Improved electrical conductivity, electrical switching, and tuning properties. *Carbohydr. Polym.* **186**, 35–44 (2018).

13. D. Pani, A. Dessì, J. F. Saenz-Cogollo, G. Barabino, B. Fraboni, A. Bonfiglio, Fully textile, PEDOT:PSS based electrodes for wearable ECG monitoring systems. *IEEE Trans. Biomed. Eng.* **63**, 540–548 (2016).

14. Y. Ding, M. A. Invernale, G. A. Sotzing, Conductivity trends of PEDOT-PSS impregnated fabric and the effect of conductivity on electrochromic textile. *ACS Appl. Mater. Interfaces* **2**, 1588–1593 (2010).

15. A. Ahmed, M. A. Jalil, M. M. Hossain, M. Moniruzzaman, B. Adak, M. T. Islam, M. S. Parvez, S. Mukhopadhyay, A PEDOT:PSS and graphene-clad smart textile-based wearable electronic joule heater with high thermal stability. *J. Mater. Chem. C* **8**, 16204–16215 (2020).

16. Y. Ding, J. Yang, C. R. Tolle, Z. Zhu, Flexible and compressible PEDOT:PSS@Melamine conductive sponge prepared *via* one-step dip coating as piezoresistive pressure sensor for human motion detection. *ACS Appl. Mater. Interfaces* **10**, 16077–16086 (2018).

17. I. Nuramdhani, M. Jose, P. Samyn, P. Adriaensens, B. Malengier, W. Deferme, G. D. Mey, L. V. Langenhove, Charge-discharge characteristics of textile energy storage devices having different PEDOT:PSS ratios and conductive yarns configuration. *Polymer* **11**, 345 (2019).

18. I. del Agua, D. Mantione, U. Ismailov, A. Sanchez-Sanchez, N. Aramburu, G. G. Malliaras, D. Mecerreyes, E. Ismailova, DVS-crosslinked PEDOT:PSS free-standing and textile electrodes toward wearable health monitoring. *Adv. Mater. Technol.* **3**, 1700322 (2018).

19. H. Shi, C. Liu, Q. Jiang, J. Xu, Effective approaches to improve the electrical conductivity of PEDOT:PSS: A review. *Adv. Electron. Mater.* **1**, 1500017 (2015).

20. M. Åkerfeldt, M. Strååt, P. Walkenström, Electrically conductive textile coating with a PEDOT-PSS dispersion and a polyurethane binder. *Text. Res. J.* **83**, 618–627 (2013).

21. M. G. Tadesse, D. A. Mengistie, Y. Chen, L. Wang, C. Loghin, V. Nierstrasz, Electrically conductive highly elastic polyamide/lycra fabric treated with PEDOT:PSS and polyurethane. *J. Mater. Sci.* **54**, 9591–9602 (2019).

22. J. D. Ryan, D. A. Mengistie, R. Gabrielsson, A. Lund, C. Müller, Machine-washable PEDOT:PSS dyed silk yarns for electronic textiles. *ACS Appl. Mater. Interfaces* **9**, 9045–9050 (2017).

23. K. K. Gleason, *CVD Polymers: Fabrication of Organic Surfaces and Devices* (John Wiley & Sons, 2015).

24. M. H. Gharahcheshmeh, M. M. Tavakoli, E. F. Gleason, M. T. Robinson, J. Kong, K. K. Gleason, Tuning, optimization, and perovskite solar cell device integration of ultrathin poly(3,4-ethylenedioxythiophene) films *via* a single-step all-dry process. *Sci. Adv.* **5**, eaay0414 (2019).

25. M. H. Gharahcheshmeh, K. K. Gleason, Device fabrication based on oxidative chemical vapor deposition (oCVD) synthesis of conducting polymers and related conjugated organic materials. *Adv. Mater. Interfaces* **6**, 1801564 (2019).

26. L. Krieg, F. Meierhofer, S. Gorny, S. Leis, D. Splith, Z. Zhang, H. von Wenckstern, M. Grundmann, X. Wang, J. Hartmann, C. Margenfeld, I. M. Clavero, A. Avramescu, T. Schimpke, D. Scholz, H.-J. Lugauer, M. Strassburg, J. Jungclaus, S. Bornemann, H. Spende, A. Waag, K. K. Gleason, T. Voss, Toward three-dimensional hybrid inorganic/organic optoelectronics based on GaN/oCVD-PEDOT structures. *Nat. Commun.* **11**, 5092 (2020).

27. G.-L. Xu, Q. Liu, K. K. S. Lau, Y. Liu, X. Liu, H. Gao, X. Zhou, M. Zhuang, Y. Ren, J. Li, M. Shao, M. Ouyang, F. Pan, Z. Chen, K. Amine, G. Chen, Building ultraconformal protective layers on both secondary and primary particles of layered lithium transition metal oxide cathodes. *Nat. Energy* **4**, 484–494 (2019).

28. M. H. Gharahcheshmeh, C. T.-C. Wan, Y. A. Gandomi, K. V. Greco, A. Forner-Cuenca, Y.-M. Chiang, F. R. Brushett, K. K. Gleason, Ultrathin conformal oCVD PEDOT coatings on carbon

electrodes enable improved performance of redox flow batteries. *Adv. Mater. Interfaces* **7**, 2000855 (2020).

29. S. Lee, K. K. Gleason, Enhanced optical property with tunable band gap of cross-linked PEDOT copolymers *via* oxidative chemical vapor deposition. *Adv. Funct. Mater.* **25**, 85–93 (2015).

30. G. Drewelow, H. Wook Song, Z.-T. Jiang, S. Lee, Factors controlling conductivity of PEDOT deposited using oxidative chemical vapor deposition. *Appl. Surf. Sci.* **501**, 144105 (2020).

31. S. G. Im, K. H. Gleason, Systematic control of the electrical conductivity of Poly(3,4-ethylenedioxythiophene) via oxidative chemical vapor deposition. *Macromolecuels* **40**, 6552–6556 (2007).

32. S. Lee, D. C. Paine, K. K. Gleason, Heavily doped poly(3,4-ethylenedioxythiophene) thin films with high carrier mobility deposited using oxidative CVD: Conductivity stability and carrier transport. *Adv. Funct. Mater.* **24**, 7187–7196 (2014).

33. S. Liu, T. Hua, X. Luo, N. Y. Lam, X.-M. Tao, L. Li, A novel approach to improving the quality of chitosan blended yarns using static theory. *Text. Res. J.* **85**, 1022–1034 (2015).

34. M. Beccatelli, M. Villani, F. Gentile, L. Bruno, D. Seletti, D. M. Nikolaidou, M. Culiolo, A. Zappettini, N. Coppedè, All-polymeric pressure sensors based on PEDOT:PSS-modified polyurethane foam. *ACS Appl. Polym. Mater.* **3**, 1563–1572 (2021).

35. P. Zhao, R. Zhang, Y. Tong, X. Zhao, T. Zhang, Q. Tang, Y. Liu, Strain-discriminable pressure/proximity sensing of transparent stretchable electronic skin based on PEDOT:PSS/SWCNT electrodes. *ACS Appl. Mater. Interfaces* **12**, 55083–55093 (2020).

36. Z. Li, S. Zhang, Y. Chen, H. Ling, L. Zhao, G. Luo, X. Wang, M. C. Hartel, H. Liu, Y. Xue, R. Haghniaz, K. Lee, W. Sun, H. Kim, J. Lee, Y. Zhao, Y. Zhao, S. Emaminejad, S. Ahadian, N. Ashammakhi, M. R. Dokmeci, Z. Jiang, A. Khademhosseini, Gelatin methacryloyl-based tactile sensors for medical wearables. *Adv. Funct. Mater.* **30**, 2003601 (2020).

37. T. Chen, S.-H. Zhang, Q.-H. Lin, M.-J. Wang, Z. Yang, Y.-L. Zhang, F.-X. Wang, L.-N. Sun, Highly sensitive and wide-detection range pressure sensor constructed on a hierarchical-structured conductive fabric as a human–machine interface. *Nanoscale* **12**, 21271–21279 (2020).

38. J. J. Lee, S. Gandla, B. Lim, S. Kang, S. Kim, S. Lee, S. Kim, Alcohol-based highly conductive polymer for conformal nanocoatings on hydrophobic surfaces toward a highly sensitive and stable pressure sensor. *NPG Asia Mater.* **12**, 65 (2020).

39. Y.-T. Tseng, Y.-C. Lin, C.-C. Shih, H.-C. Hsieh, W.-Y. Lee, Y.-C. Chiu, W.-C. Chen, Morphology and properties of PEDOT:PSS/soft polymer blends through hydrogen bonding interaction and their pressure sensor application. *J. Mater. Chem. C* **8**, 6013–6024 (2020).

40. L. Sun, S. Jiang, Y. Xiao, W. Zhang, Realization of flexible pressure sensor based on conductive polymer composite *via* using electrical impedance tomography. *Smart Mater. Struct.* **29**, 055004 (2020).

41. Y. Li, C. Jiang, W. Han, Extending the pressure sensing range of porous polypyrrole with multiscale microstructures. *Nanoscale* **12**, 2081–2088 (2020).

42. J.-C. Wang, R. S. Karmakar, Y.-J. Lu, S.-H. Chan, M.-C. Wu, K.-J. Lin, C.-K. Chen, K.-C. Wei, Y.-H. Hsu, Miniaturized flexible piezoresistive pressure sensors: Poly(3,4-ethylenedioxythiophene):poly(styrenesulfonate) copolymers blended with graphene oxide for biomedical applications. *ACS Appl. Mater. Interfaces* **11**, 34305–34315 (2019).

43. Z. Wang, Y. Si, C. Zhao, D. Yu, W. Wang, G. Sun, Flexible and washable poly(ionic liquid) nanofibrous membrane with moisture proof pressure sensing for real-life wearable electronics. *ACS Appl. Mater. Interfaces* **11**, 27200–27209 (2019).

44. Y.-J. Tsai, C.-M. Wang, T.-S. Chang, S. Sutradhar, C.-W. Chang, C.-Y. Chen, C.-H. Hsieh, W.-S. Liao Multilayered Ag NP-PEDOT-paper composite device for human-machine interfacing. *ACS Appl. Mater. Interfaces* **11**, 10380–10388 (2019).

45. J. Oh, J.-H. Kim, K. T. Park, K. Jo, J.-C. Lee, H. Kim, J. G. Son, Coaxial struts and microfractured structures of compressible thermoelectric foams for self-powered pressure sensors. *Nanoscale* **10**, 18370–18377 (2018).

46. O. Y. Kweon, S. J. Lee, J. H. Oh, Wearable high-performance pressure sensors based on three-dimensional electrospun conductive nanofibers. *NPG Asia Mater.* **10**, 541–551 (2018).

47. K. Qi, J. He, H. Wang, Y. Zhou, X. You, N. Nan, W. Shao, L. Wang, B. Ding, S. Cui, A highly stretchable nanofiber-based electronic skin with pressure-, strain-, and Flexion-Sensitive properties for health and motion Monitoring. *ACS Appl. Mater. Interfaces* **9**, 42951–42960 (2017).

48. C. Pang, G.-Y. Lee, T. Kim, S. M. Kim, H. N. Kim, S.-H. Ahn, K.-Y. Suh, A flexible and highly sensitive strain-gauge sensor using reversible interlocking of nanofibres, *Nat. Mater.* **11**, 795–801 (2012).

49. W. W. Nichols, Clinical measurement of arterial stiffness obtained from noninvasive pressure waveforms. *Am. J. Hypertens.* **18**, 3S–10S (2005).

50. J. Park, J. Kim, J. Hong, H. Lee, Y. Lee, S. Cho, S.-W. Kim, J J. Kim, S. Y. Kim, H. Ko, Tailoring force sensitivity and selectivity by microstructure engineering of multidirectional electronic skins. *NPG Asia Mater.* **10**, 163–176 (2018).

51. C. Dagdeviren, Y. Su, P. Joe, R. Yona, Y. Liu, Y.-S. Kim, Y. A. Huang, A. R. Damadoran, J. Xia, L. W. Martin, Y. Huang. J. A. Rogers, Conformable amplified lead zirconate titanate sensors with enhanced piezoelectric response for cutaneous pressure monitoring. *Nat. Commun.* **5**, 4496 (2014).

52. F. Q. Al-Khalidi, R. Saatchi, D. Burke, H. Elphick, S. Tan, Respiration rate monitoring methods: A review, *Pediatr. Pulmonol.* **46**, 523–529 (2011).

53. S. Fleming, T. DPhil, R. Stevens, C. Heneghan, A. Plüddemann, I. Maconochie, L. Tarassenko, D. Mant, Normal ranges of heart rate and respiratory rate in children from birth to 18 years of age: A systematic review of observational studies. *Lancet* **377**, 1011–1018 (2011).

54. S. D. Kelly, M. A. E. Ramsay, Respiratory rate monitoring: Characterizing performance for emerging technologies. *Anesth. Analg.* **119**, 1246–1248 (2014).

55. A. Rodríguez-Molinero, L. Narvaiza, J. Ruiz, C. Gálvez-Barrón, Normal respiratory rate and peripheral blood oxygen saturation in the elderly population. *J. Am. Geriatr. Soc.* **61**, 2238–2240 (2013).

56. P. Kovacik, G. Hierro, W. Livernois, K. K. Gleason, Scale-up of oCVD: Large-area conductive polymer thin films for next-generation electronics. *Mater. Horiz.* **2**, 221–227 (2015).

57. L. K. Allison, T. L. Andrew, A wearable all-fabric thermoelectric generator. *Adv. Mater. Technol.,* **4**, 1800615 (2019).